ACS OMEGA

http://pubs.acs.org/journal/acsodf

Article

Carboxylated PEG-Functionalized $MnFe_2O_4$ Nanocubes Synthesized in a Mixed Solvent: Morphology, Magnetic Properties, and Biomedical Applications

Chandunika R. Kalaiselvan, Nanasaheb D. Thorat, and Niroj Kumar Sahu*

Cite This: *ACS Omega* 2021, 6, 5266−5275

Read Online

ACCESS | Metrics & More | Article Recommendations | Supporting Information

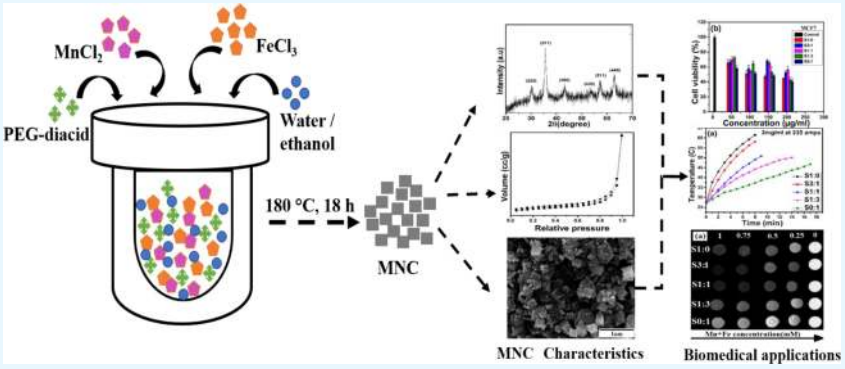

ABSTRACT: Ferrites are one of the most studied materials around the globe due to their distinctive biological and magnetic properties. In the same line, anisotropic $MnFe_2O_4$ nanoparticles have been explored as a potential candidate possessing excellent magnetic properties, biocompatibility, and strong magnetic resonance imaging (MRI) properties such as $r2$ relaxivity for magnetic field-guided biomedical applications. The current work reports the synthesis and morphological evolution of $MnFe_2O_4$ nanocubes (MNCs) in a hydrothermal process using different volume ratios of water and ethanol. The synthesis protocol was designed to influence the properties of the ferrite nanocubes, for example, the variation in surface tension, dielectric properties, and the ionic character of the solvent, and this has been achieved by adding ethanol into water during the synthesis. Pristine $MnFe_2O_4$ is formed with well-defined cubic to irregular cubic shapes with the addition of ethanol, as evidenced from XRD, field emission scanning electron microscopy, and porosity measurements. MNCs have been investigated for magnetic hyperthermia and MRI applications. Well-defined cubic-shaped MNCs with uniform size distribution possessed a high saturation magnetization of 63 emu g^{-1} and a transverse relaxivity ($r2$) of 216 mM^{-1} s^{-1} (Mn + Fe). Furthermore, the colloidal nanocubes showed concentration-dependent hyperthermic response under an alternating magnetic field. The MNCs are biocompatible but advantageously show anticancer activities on breast cancer MCF 7 and MDA-MB-231 cells.

1. INTRODUCTION

Recent advances in nanoscale materials have paved the way for augmenting progress in the field of cancer theranostics.[1] Among nanoscale materials, magnetic nanoparticles (MNPs) are extensively being investigated for cancer diagnosis and therapy. Magnetic materials are classified as dia, para, ferri, ferro, and antiferromagnetic materials based on their magnetic properties. At nanoscale dimensions, ferro and ferri MNPs exhibit superparamagnetic behavior below a critical size, which is beneficial for biomedical applications such as magnetic hyperthermia, magnetically guided and activated drug delivery, and magnetic resonance (MR) imaging (MRI). Among superparamagnetic nanoparticles, ferrite-based MNPs (MFe_2O_4, where M = Fe, Mn, Co, Ni, Zn, etc.) are commonly employed. Moreover, these materials are studied for various applications such as drug delivery and T_2 contrast for MRI and as hyperthermia agents.[2−8] A comparative MRI study of different metal-doped ferrite-based MNPs ($MnFe_2O_4$, $FeFe_2O_4$, $CoFe_2O_4$, and $NiFe_2O_4$) was performed by Lee *et al.*[9] and found that $MnFe_2O_4$ with higher magnetization and magnetic susceptibility exhibited better performance. The mangafodipir trisodium (MnDPDP, teslascan)−Mn^{2+}-containing contrast agent has been used in clinical studies for hepatic MRI,[10] and Mn(II) chloride (LumenHance) has been used as an oral contrast agent.[11] The shape, size, particle size

Received: November 4, 2020
Accepted: January 12, 2021
Published: February 18, 2021

distribution, and surface coating of MNPs play a significant role in biological applications.[12] Therefore, the synthesis of MNPs with a uniform shape and size is of scientific importance. There are many reports on the shape-selective synthesis of MNPs such as rods, cubes, octopods, tetrapods, disks, rhombohedrons, and so forth.[13−19] The shape and size of MNPs significantly change their physicochemical properties. For example, the size of the iron oxide nanoparticle determines its ferromagnetic or superparamagnetic behavior due to the size-dependent spin-exchange effect, while shape-induced magnetocrystalline anisotropy switches the properties of MNPs.[20−22] It is reported that MNPs with shape anisotropy have greater performance when used in T_2-weighted MRI due to their effective radii.[23−25]

At present, many aqueous and nonaqueous synthesis methods such as chemical co-precipitation,[26] microemulsion,[27] thermal decomposition,[28] polyols,[29] hydrothermal,[30] and sonochemical[31] have been used to prepare MNPs. Among the aqueous methods, the chemical co-precipitation process is carried out at low temperature and hence mostly adopted. In this synthesis method, MNPs are formed at a pH of around 10−11. However, the ferrite solution containing Fe^{2+} and Fe^{3+} has a pH value of 1−2. Thus, to maintain the basicity, solutions of NaOH or KOH or NH_4OH etc. are certainly added to the ferrite solution.[32] Nonhomogeneity of this solution is a hindrance for the formation of uniform-sized particles, which is considered as a major drawback of this method. In the nonaqueous method, high-temperature organic phase synthesis of MNPs has been commonly employed as it gives a narrow distribution of particle size range of up to 20 nm.[33−35] However, MNPs synthesized by this method are hydrophobic, and hence, phase transfer of MNPs is a necessary step for biological applications. These difficulties suggest a different approach to synthesize size and property-tunable MNPs dispersible in aqueous solutions for further use in biological applications.[36]

In this work, a facile solvothermal approach has been adopted to synthesize cubical-shaped poly(ethylene glycol) (PEG)-diacid-functionalized $MnFe_2O_4$ nanoparticles. Here, the solvothermal synthesis route used is analogous to the hydrothermal method, except for the use of ethanol as a solvent instead of water alone. The morphology of MNCs changes with the variation in the proportion of the reaction solvent from water to ethanol. The synthesized MNCs are evaluated for cytotoxicity, MRI, and hyperthermia studies.

2. CHARACTERIZATION TECHNIQUES USED

The crystal structure of the nanoparticles was examined using a powder XRD (X-ray diffractometer) D8 ADVANCE Bruker diffractometer using a Cu Kα radiation source at 40 kV. The crystallite sizes were calculated using $d = k\lambda/(\beta\cos\theta)$, Debye−Scherrer's equation, where λ = 1.5406 Å, k = 0.9, β = full width at half-maximum (FWHM), and θ = diffraction angle. Structural refinements using the Rietveld method were carried out by the PDXL-2 program. Field emission scanning electron microscopy (FESEM) was used to record the microstructure of the samples employing a Carl Zeiss Neon-40 field emission scanning electron microscope. The magnetic parameters of MNCs were measured at room temperature (300 K) using a vibrating sample magnetometer (VSM, Lake Shore). Fourier transform infrared (FTIR) spectra of the samples were recorded in the range of 400−4000 cm^{-1} using a Shimadzu IR Prestige instrument. The hydrodynamic size and colloidal stability of the samples were measured using a dynamic light scattering (DLS) Litesizer 500 particle size analyzer. A Quantachrome Nova Station 1000 instrument was used for measuring the BET surface area, porosity, and pore size distribution of the samples by the adsorption and desorption behaviors of nitrogen gas (77 K).

2.1. *In Vitro* Studies on Breast Cancer (MCF-7 and MDA-MB-231) Cell Lines. The cytotoxicity studies were carried out using nontumorigenic epithelial cells (MCF-10) and breast cancer cells (MCF-7 and MDA-MB-231). Normal epithelial cells were cultured in Dulbecco's modified Eagle's medium (DMEM) with (100 U) 20 μg mL^{-1} penicillin, 100 μg mL^{-1} streptomycin, and 10% fetal bovine serum (FBS). MCF7 and MDA-MB-231 cells were cultured in Ham's F12 and DMEM in a 1:1 ratio mixture with 0.01 mg mL^{-1} insulin, 100 μg mL^{-1} cholera toxins, 500 μg mL^{-1} hydrocortisone, 20 mg mL^{-1} of the epidermal growth factor (EGF), and 5% chelex-treated horse serum. The cells were seeded in 96-well flat-bottom titer plates at a density of 5000 cells per well and incubated for 48 h at 37 °C in a 5% CO_2 atmosphere.

The cells were treated with different metal ion concentrations of MNCs (25, 50, 100, and 200 μg mL^{-1} dissolved in DMSO) and incubated for 48 h. The wells without the nanoparticle treatment were used as the control, and the cytotoxicity effect was determined by the 3-(4,5-dimethylthiazol-2-yl)-2,5-diphenyl tetrazolium bromide (MTT) assay. After incubation, the wells were washed twice using PBS. Then, 100 μL of the MTT dye in DMEM was added and incubated for another 2 h. Finally, 100 μL of the MTT lysis buffer was added and incubated for 2 h. At 570 nm, the absorbance was measured using a microplate reader. The cell viability was calculated by measuring the optical density (OD) using eq 1

$$\text{cell viability}(\%) = \frac{\text{mean OD}}{\text{control OD}} \times 100\% \quad (1)$$

2.2. Magnetic Hyperthermia. The magnetic hyperthermia (MHT) measurements were carried out by placing the MNP dispersion in an alternating magnetic field (AMF) generated using an Ambrell Easyheat-8310, 4.2 kW system. The dispersion was kept in a 2 mL vial and placed inside an induction coil of a diameter of 0.034 m. The rise in the temperature of the sample was measured using the temperature probe (optical fiber). The specific absorption rate (SAR) values of the samples with different concentrations of 0.5, 1, and 2 mg mL^{-1} were calculated from the slope of the time versus temperature plot by using eq 2

$$\text{SAR} = C_{\text{Water}} \times \frac{1}{m} \times \frac{\Delta T}{\Delta t} \quad (2)$$

where C_{Water} is the specific heat of water which is equal to 4.18 J g^{-1} $°C^{-1}$, m is the mass of the MNPs in the aqueous suspension, and $\Delta T/\Delta t$ is the initial slope of the temperature curve.

2.3. *In Vitro* Magnetic Resonance Imaging Using Phantom Agar Gels. A BRUKER (7 T) Animal MRI-BioSpec-70/30-USR was used for the relaxivity measurement. For the MRI contrast study, the relaxivity measurement of the magnetic material was compared with respect to the proton relaxation rate. To measure the transverse relaxation ($r2$), suspensions with various concentrations (metal ions, Mn + Fe) from 0 to 1 mM of MNCs were prepared in agarose gel. T_2 relaxation times were obtained using a multiecho multislice

https://dx.doi.org/10.1021/acsomega.0c05382
ACS Omega 2021, 6, 5266−5275

sequence. To measure T_2 relaxations, the parameters such as repetition time (TR) = 2500 ms, echo time (TE) = 33 ms, field of view = 8 mm, thickness = 1.5 mm, and matrix resolution = 256 × 256 pixels were used.

3. RESULTS AND DISCUSSION

3.1. Structural, Microstructural, and Surface Properties. The intensities and relative position of the diffraction peaks in XRD patterns of different MNCs confirm the formation of $MnFe_2O_4$ (Figure 1a). The relative intensities

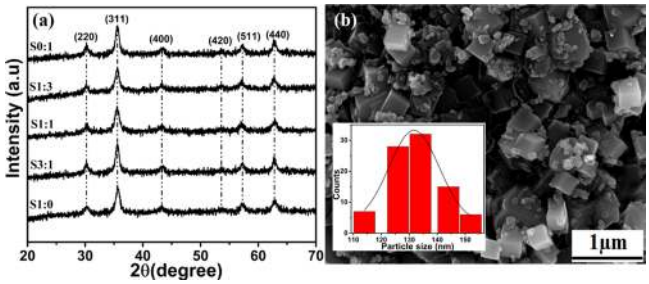

Figure 1. (a) XRD patterns of MNCs and (b) FESEM image with the inset graph representing particle size distribution for the sample S1:0.

and their peak positions are found to be similar. The diffraction peaks at 2θ values of 29.7, 34.9, 42.5, 52.6, 56.2, and 64.7° match with the (220), (311), (400), (422), (511), and (440) planes of the face-centered cubic spinel structure of $MnFe_2O_4$ (JCPDS 74-2403), respectively. The absence of any extra peaks indicates that no secondary phases are present. No crystalline peak in XRD patterns due to surface coating is observed. The crystallite sizes are found to be 33 ± 2.1, 35 ± 1.5, 37 ± 2, 30 ± 1.2, and 30 ± 0.8 nm for the samples S1:0, S3:1, S1:1, S1:3, and S0:1, respectively. Rietveld refinement was carried out using PDXL 2 software for crystalline properties. The cubic phase and *Fd*-3*m* space group have been considered for refinement. Figure S1 and Table S1 show the Rietveld refinement XRD analysis and reliability factors of the samples. The goodness of fit S = Rwp/Re, where Rwp and Re are, respectively, the R-weighted and R-expected patterns. The low value of goodness of fit in all cases justifies the goodness of refinement. The crystallite sizes obtained from Rietveld are 28.9, 31.4, 35.2, 26.8, and 26 nm, which are very close to the calculated values. It was inferred that crystallite size varied with ethanol concentration. This may be due to the role of the solvent during the synthesis process of nanoparticles. It is well known that the dielectric constant and surface tension of different solvents are different. The surface tensions of water and ethanol at 25 °C are 77.82 and 22.39 dyn cm^{-1}, respectively; however, the respective dielectric constants at 20 °C are 80.1 and 25.3.[37] Addition of ethanol to water changes the dielectric constant of the solvent and affects the colloidal interaction between particles.[38]

By classical nucleation theory,[39] the formation of particles depends on the supersaturation (S) of the solute and is given by

$$S = \frac{C}{C_i} \tag{3}$$

where C is the solute concentration and C_i is the saturation concentration. The supersaturation can be achieved by changing the pH of the reaction, evaporation of the solvent, lowering of temperature, the composition of the solvent, etc.[40] The more significant number of nuclei formed when the S value was larger than unity. The Gibbs free energy (ΔG^*) from the supersaturated state to the equilibrium state at a temperature T is given by

$$\Delta G^* = \frac{16\pi\nu^2\gamma^3}{3(kT)^2(\ln S)^2} \tag{4}$$

where γ is the surface energy per unit area and ν is the molecular volume of the solute. The nucleation rate can be determined by substituting eq 4 into the Arrhenius rate equation which is given by

$$J = J_o \exp\left[-\frac{16\pi\nu^2\gamma^3}{3(kT)^3(\ln S)^2}\right] \tag{5}$$

where k is Boltzmann's constant, T is the Kelvin temperature, J is the nucleation rate, and J_o is the rate constant. Equation 5 dictates that the nucleation increases with the degree of supersaturation. Additionally, by the Kelvin equation,[39] the relationship between the nuclei radius and the supersaturation can be expressed as

$$\ln S = \frac{2m\gamma}{rkT_\rho} \tag{6}$$

The equilibrium concentration of the solute in the saturated solution is given by

$$C_{\text{liquid}} \approx \exp\left[-\frac{z + z - e^2}{4\pi\varepsilon_0\varepsilon kT(r_+ + r_-)}\right] \tag{7}$$

where ε_0 is the permittivity in vacuum and ε is the dielectric constant in a given solution. The symbols r_+ and r_ represent the radii of ions having respective charges of z_+ and z_-.[41] The combination of eqs 3, 6, and 7 results in

$$\frac{2m\gamma}{rkT_\rho} = \ln C + \frac{z + z - e^2}{4\pi\varepsilon_0\varepsilon kT(r_+ + r_-)} \tag{8}$$

Hence, the relation between the dielectric constant and particle radius can be written as

$$\frac{1}{r} = A + \frac{B}{\varepsilon} \tag{9}$$

where $A = kT_\rho/2m\gamma \ln C$ and $B = \rho z + z - e^2/8\pi m\gamma\varepsilon_0(r_+ + r_-)$.

In the mixed solvent, A and B are constants, and therefore, if the dielectric constant of the solvents changes, there will be a change in supersaturation which affects the nucleation and particle sizes.

Surface coating of MNCs with PEG-diacid was studied by FTIR absorption spectra. FTIR spectra of all the samples are shown in Figure S2. The corresponding peaks of PEG-diacid observed at 1610 cm^{-1} are due to the $-COO^-$ asymmetric stretching of the COOH group in PEG-diacid. Further symmetric stretching observed at 1421 cm^{-1} due to the vibrational mode of $-COO^-$ and at 1075 cm^{-1} due to the carboxylic C−OH bending vibration mode confirms the presence of PEG-diacid on the MNC nanoparticles. The presence of a hydrogen bond was confirmed by the O−H stretching vibration of the hydroxyl group at 3342 cm^{-1}. The strong absorption band at 520 cm^{-1} is attributed to metal oxide (Fe−O and Mn−O) vibrations.[42−44] The presence of

https://dx.doi.org/10.1021/acsomega.0c05382
ACS Omega 2021, 6, 5266−5275

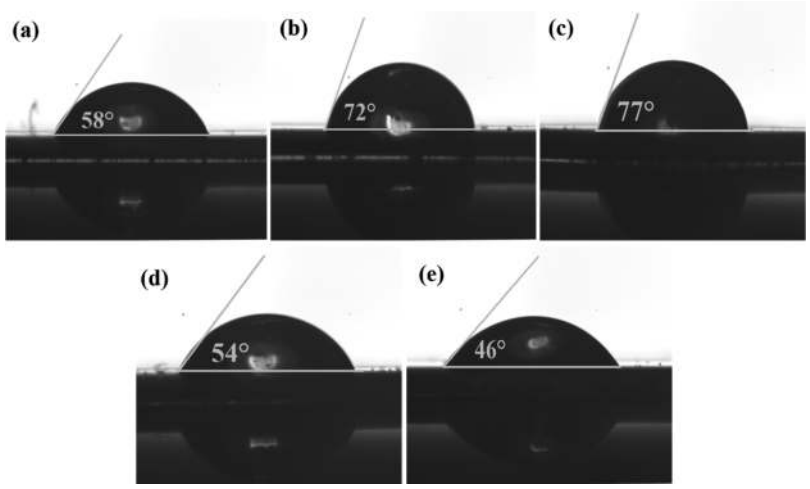

Figure 2. Contact angle measurement of MNCs; (a) S1:0, (b) S3:1, (c) S1:1, (d) S1:3, and (e) S0:1.

the above vibrational bands confirms the formation and surface functionalization of MNCs.

For biological applications such as drug delivery, hyperthermia, and MR imaging, the MNPs should neither aggregate nor disintegrate and should possess good colloidal dispersion. To study this, the DLS experiment was carried out for MNCs at room temperature. The hydrodynamic diameter and zeta potential were measured in deionized (DI) water. Table S2 gives the zeta potential values (in the range from −25 to −33 mV) for all samples which assure the highly stable nature of MNCs at room temperature, validating the presence of surface coating. The hydrodynamic diameters of MNCs in DI water are found to be in the range of ∼200 to 300 nm (Figure S3). The hydrodynamic size and zeta potential value ensure that the nanoparticles are highly stable for biomedical applications. The hydrophilic and wettability nature of MNCs was studied by measuring the contact angle of the colloidal sample. The hydrophilicity nature of nanoparticles plays a significant role in steric stabilization which is quantified in terms of contact angle. Surfaces with contact angles greater than 90° are hydrophobic in nature, whereas surfaces with contact angles less than 90° are categorized as hydrophilic. Figure 2 depicts the static contact angle of 46 to 77°, implying the hydrophilic nature of the MNCs. The main advantage of the use of PEG-diacid is that it provides a hydrophilic surface to MNCs which gives a stable colloidal suspension beneficial for *in vitro* or *in vivo* applications. PEG-diacid is relatively nontoxic to the cellular system, and large quantities are absorbed in cellular membranes. This is because PEG is known to associate with membrane phospholipid headgroups and in process such as protein purification.[45,46] MNCs with the PEG-diacid surface can be used directly without further phase transfer for biological applications such as hyperthermia and MRI.

The microstructural size and surface morphology of MNCs were calculated and analyzed from FESEM images, and the particle size distribution was calculated using the Gaussian function. From FESEM images, the variation in the average size of MNCs with the addition of ethanol is clearly seen, which shows that the size of the MNCs can be manipulated by adjusting the solvent ratio in the reaction. The FESEM image of S1:0, as shown in Figure 1b, with no ethanol in the solvent, shows a cubic shape with an average diameter of 135 nm. Agglomeration seen in the images may be due to the magnetic dipolar interaction and van der Waals force among particles. The TEM image of the S1:0 sample is included in the Supporting Information, Figure S7, which confirms the formation of the cubical shape. When the concentration of ethanol in the solvent is increased, as in the case of 3:1 and 1:1 ratios, an increase in average particle size (Figure 3a,b) and

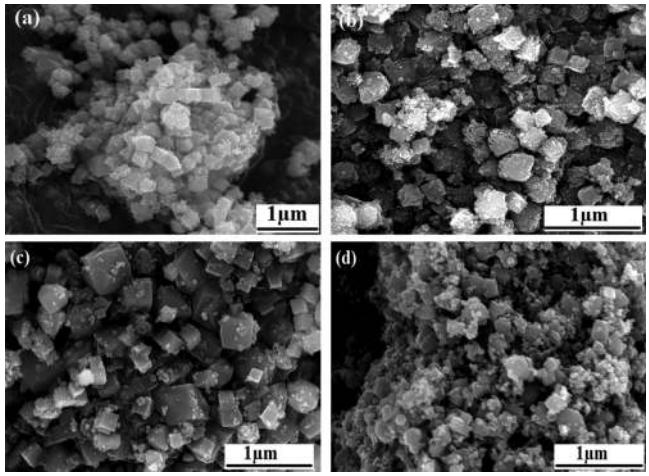

Figure 3. FESEM images of (a) S3:1, (b) S1:1, (c) S1:3, and (d) S0:1 showing variation in the shape of the nanoparticles with the amount of added ethanol.

Supporting Information Figure S4) is observed and found to be 140 and 147 nm, respectively, due to the increase in the nucleation of manganese ferrite in the solution. In general, the growth of the metal oxide takes place in two stages, which involves nucleation of the primary particles and aggregation. Basically, nucleation depends on the rate of dissolution of an ionic compound in a solvent. Based on the electrostatic model proposed by Burger,[47] the chemical potential of the phase when the solute precipitates from a supersaturated ideal state into a solution is given by

$$\mu^{\circ}_{\text{solid}} + kT\ln C_{\text{solid}} = \mu^{\circ}_{\text{liquid}} + kT\ln C_{\text{liquid}} \quad (10)$$

where "solid" and "liquid" in the subscripts stand for the solid phase and liquid phase, respectively, μ° is the standard chemical potential, k is Boltzmann's constant, T is the Kelvin temperature, and C is the concentration of the solute. The

https://dx.doi.org/10.1021/acsomega.0c05382
ACS Omega 2021, 6, 5266−5275

energy required to separate the charged ions from the ideal solid state is given by Coulomb's interaction[41]

$$\Delta\mu^{\circ} \approx \frac{z + z - e^2}{4\pi\varepsilon_0\varepsilon(r_+ + r_-)} \quad (11)$$

The symbols $z+$ and $z-$ are charged ions with the radii of $r+$ and $r-$, respectively, ε is the dielectric constant in a given solution, ε_0 is the permittivity in vacuum, and e (elementary charge) = 1.602×10^{-19} C. The equilibrium concentration of the solute in the saturated solution is given by combining the above equations

$$C_{\text{liquid}} \approx \exp\left[-\frac{z + z - e^2}{4\pi\varepsilon_0\varepsilon kT(r_+ + r_-)}\right] \quad (12)$$

From the equation, the dielectric constant (ε) of the solution is inversely proportional to the logarithm of the equilibrium concentration of the solute, that is, ln C_{liquid}. This shows that when the dielectric constant of the solution is higher, the solubility (C_{liquid}) is large; hence, the nucleation is high. Thus, the solubility of the precursor in water is larger, resulting in a faster release of OH^- ions, and more nuclei formed explain the increase in the size of MNC nanoparticles with an increase in the amount of ethanol. However, further addition of ethanol to the solvent, for example, in 1:3 and 0:1 ratios, samples S1:3 and S0:1 exhibit irregular shapes with particle sizes of 122 and 113 nm, respectively (Figure 3c,d). When excess ethanol is added to the reaction solvent, hydroxyl groups exist on the surface of the precursor, which adsorbs ethanol molecules *via* hydrogen bond formation. As the addition of ethanol increases in the solvent, the adsorption of ethanol increases on the surface, which decreases the solubility of the precursor. As a result, when there were more ethanol molecules on the surface, the dissolution−crystallization process of the precursor was inhibited by the growth and coalition of the particles, leading to smaller-size MNCs.[48] Thus, the polarity of the solvent has a significant influence on the shape and size the nanoparticles.

N_2 adsorption−desorption isotherm measurements were carried out to investigate the pores in the nanoparticles, as shown in Figure S5. The isotherms of nanoparticles exhibit a type IV isotherm resembling H2 hysteresis. Such a hysteresis loop is due to the microporous nature of the samples as per IUPAC classification.[49] These loops are observed at high relative pressures in the range of 0−1.0, which suggest the pore formation due to the loose arrangement of particles. For all the samples, the average pore diameters are found to be ∼1.4 nm. Usually, the loops appear due to the capillary condensation from micropores to macropores at relatively high pressure. BET results show that all the samples have a microporous structure, and even from FESEM images, no macropores were seen. The values obtained from the BET analysis are listed in Table S3 (Supporting Information). It is observed from the BET surface area (S_{BET}) data that the total pore volume first decreases and then increases with the amount of ethanol. For the sample prepared with only ethanol as a solvent, the BET surface area is found to be 72.23 $m^2\ g^{-1}$ and it can be assumed that an adequate amount of ethanol has an immense effect on improving the surface area of mesoporous nanoparticles. The BET results elucidate that the mixed solvent can affect the pore size and specific surface area.

3.2. Magnetic Properties. Magnetization (M) versus applied field (H) plots for different MNCs at room temperature are given in Figure 4. The saturation magnetization M_s, coercivity H_c, remanent magnetization M_r, and

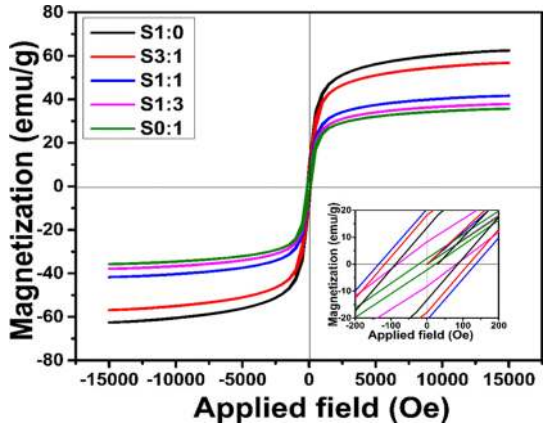

Figure 4. Hysteresis loops of different MNCs at room temperature (the inset is the magnified view).

susceptibility χ for MNCs are listed in Table 1. The S1:0 nanoparticles possessed the highest M_s of 62 emu g^{-1}, M_r of 6 emu g^{-1}, and H_c of 86 Oe, indicating a weakly ferromagnetic behavior. The M_s values of MNCs prepared with the addition of ethanol decrease and are found to be 56.96, 41.5, 37.73, and 35.59 emu g^{-1} for S3:1, S1:1, S1:3, and S0:1, respectively. Even if the saturation magnetization is an intrinsic property of the material, the M_s values of MNC are significantly lower compared to that of bulk $MnFe_2O_4$ (M_s = 80 emu g^{-1}), which may be due to the surface effect in nanomaterials. The initial magnetic susceptibility (χ_m) of the samples is calculated by the initial slope of the $M-H$ curve and is found to be $\sim 10^{-2}$ emu $g^{-1}Oe^{-1}$. Interestingly, χ_m linearly decreases with the concentration of ethanol used during the preparation of materials. For the applied fields of 444 and 565 Oe (fields utilized in hyperthermia), the susceptibilities are calculated and provided in Table 1. There are no significant decrease in susceptibilities with the application of H, which is advantageous for hyperthermia. These changes in magnetic parameters are due to variation in the microstructure, morphology, and particle size, which leads to different spin disorders at the surface.[50] By Neel's model, the magnetic moment (m) for $MnFe_2O_4$ is the magnetic moment of ions in the octahedral sites (m_B) to the magnetic moment at tetrahedral sites (m_A). Hence, the magnetic moment highly depends on the cation distribution in A and B lattices. In the present study, the addition of ethanol may result in the decrease of M_s of MNCs due to migration of Fe^{3+} and Mn^{2+} from octahedral to tetrahedral sites.[50] From the inset graph, it is observed that remanence and coercivity are dependent on the crystallite size of the sample. In general, coercivity is based on shape anisotropy, magnetocrystalline anisotropy, exchange anisotropy, etc. In this work, the variation in coercivity may be due to the shape anisotropy in the MNC. It is reported that magnetocrystalline and exchange anisotropy changes with the substitution of A- and B-site cations in $MnFe_2O_4$.[50]

3.3. Heat Generation in Magnetic Colloids. The absorption efficiency of materials to generate heat due to the applied AMF is measured in terms of the SAR. The transformation of magnetic energy into heat due to the application of AMF is governed mainly by hysteresis loss and the relaxation process. In general, relaxation types are Néel and

https://dx.doi.org/10.1021/acsomega.0c05382
ACS Omega 2021, 6, 5266−5275

Table 1. Parameters Associated with MNCs as per the Data Obtained from VSM and MRI

				χ(emu.g^{-1} Oe^{-1})			
samples	M_s (emu g^{-1})	M_r (emu g^{-1})	H_c (Oe)	initial	at 444 Oe	at 565 Oe	$r2$ (mM^{-1} s^{-1})
S1:0	62.73	6.8	86.6	0.0716	0.077	0.0631	215.72
S3:1	56.96	9.1	115.5	0.0701	0.0703	0.0579	213.68
S1:1	41.5	10.2	135.9	0.0514	0.0512	0.0428	197.12
S1:3	37.73	4.3	78.6	0.0467	0.0462	0.0376	156.84
S0:1	35.59	2.1	22.3	0.044	0.0437	0.0357	113.58

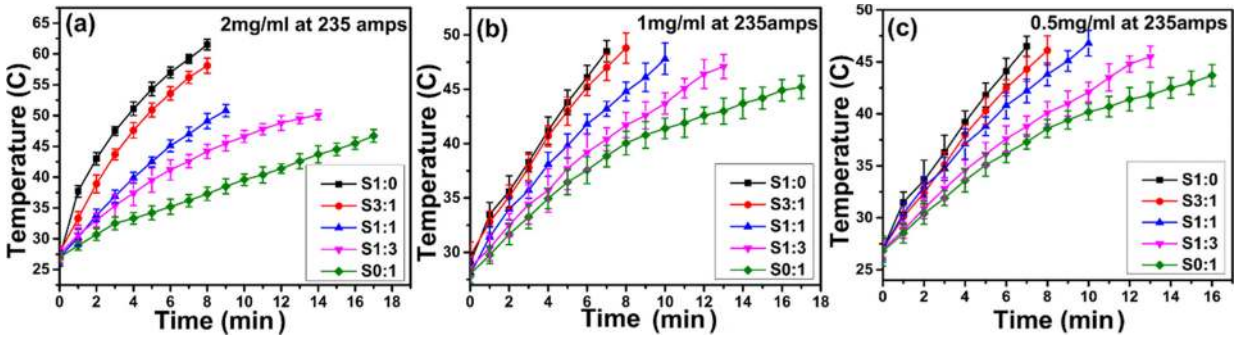

Figure 5. Time versus temperature plot of the different MNCs at different concentrations with the application of AMF of a field strength of 35.28 kA m^{-1} and a frequency of 316 kHz; (a) at 2 mg mL^{-1}, (b) at 1 mg mL^{-1}, and (c) at 0.5 mg mL^{-1}.

Table 2. SAR Values for MNCs at AMF of Different Field Strengths

	SAR in W g^{-1}					
	300 Amps			235 Amps		
samples	2 mg mL^{-1}	1 mg mL^{-1}	0.5 mg mL^{-1}	2 mg mL^{-1}	1 mg mL^{-1}	0.5 mg mL^{-1}
S1:0	391.3	195.69	158.8	322.15	161.07	137.97
S3:1	331.78	162.45	145.1	268.82	134.41	131.691
S1:1	269.15	131.90	149.8	264.97	132.48	92.95
S1:3	293.81	196.90	99.12	188.03	94.0	53.83
S0:1	121.47	64.84	55.33	132.61	66.3	37.12

Brownian relaxations. Néel relaxation occurs due to change in the magnetic moment orientation, whereas Brownian relaxation is due to the physical rotation of particles within the colloidal suspension. The phase lag occurring between AMF and the magnetic moment direction due to these relaxations tends to generate thermal losses.[51] The concentration effect on the hyperthermic response of the MNCs at various concentrations of 0.5, 1, and 2 mg mL^{-1} was examined under a 316 kHz frequency of AMF and a field strength of 35 kA m^{-1} (Figure 5). It is observed that there is a gradual increase in temperature with time upon increasing the concentration of samples. The SAR values increase significantly with concentrations (Table 2). These results suggested that there is an increase in dipolar interactions due to the concentration which leads to stabilizing the nanoparticles against re-orientation to the applied field.

In order to evaluate the effect of magnetic field intensity, the samples were taken at the concentrations of 0.5, 1, and 2 mg mL^{-1} and exposed to AMF of a field strength of 45 kA m^{-1} keeping other parameters the same at a fixed frequency of 316 kHz. For hyperthermia therapy, Atkinson and Brezovich reported the product of frequency (f) and field strength (H) as per the patient's tolerance limit to be 4.85 × 10^8 A ms^{-1}.[52] However, for clinical studies, H should be in the range of 100−400 Oe and f should be between 100 and 250 kHz, which may vary depending on heat requirement and the tumor site.[53] Here, we have used the maximum $H{\cdot}f$ value of 4.7 × 10^9 A ms^{-1} for hyperthermia measurements (Figure S6). In this work, the hyperthermia temperatures are promisingly achieved within few minutes. To calculate SAR values (W g^{-1}), the initial slope of the temperature−time graph was used, and the values are shown in Table S4. An increase in SAR value was observed as the field strength increased from 15 to 45 kA m^{-1} and found that SAR values vary with the square of the field intensity.[54] A comparison of the SAR values of $MnFe_2O_4$ nanoparticles with other reported values[55−57] suggested that the obtained SAR value for the MNCs at 235 and 300 Amps in this work shows excellent performance. In fact, the SAR values of the MNCs are comparable to those of the commercial MNPs 09-56-132 (Micromod, Germany, SAR = 183 W g^{-1}), Fluidmag/C11-D (Chemicell, Germany, SAR = 173 W g^{-1}), SEI-10-05 (Ocean NanoTech, USA, SAR = 131 W g^{-1}), and HyperMAG A (nanoTherics, UK, SAR = 396 W g^{-1}).[58]

3.4. *In Vitro* Cell Cytotoxicity. The cytotoxicity study of functionalized MNCs was carried out on two different breast cancer cell lines (MCF-7 and MDA-MB-231) and normal epithelial cell MCF-10 cell lines at different concentrations of MNCs (normalized in terms of metal ion concentrations of 25, 50, 100, and 200 μg mL^{-1}) and incubated for 48 h at 37 °C. The two different breast cancer cells are invasive and have many phenotypic/genotypic differences. MCF-7 cells are estrogen-dependent with a positive receptor, whereas MDA-MB-231 are triple-negative with an estrogen-negative receptor.[59] Hence, this study was aimed to evaluate the cytotoxic

https://dx.doi.org/10.1021/acsomega.0c05382
ACS Omega 2021, 6, 5266−5275

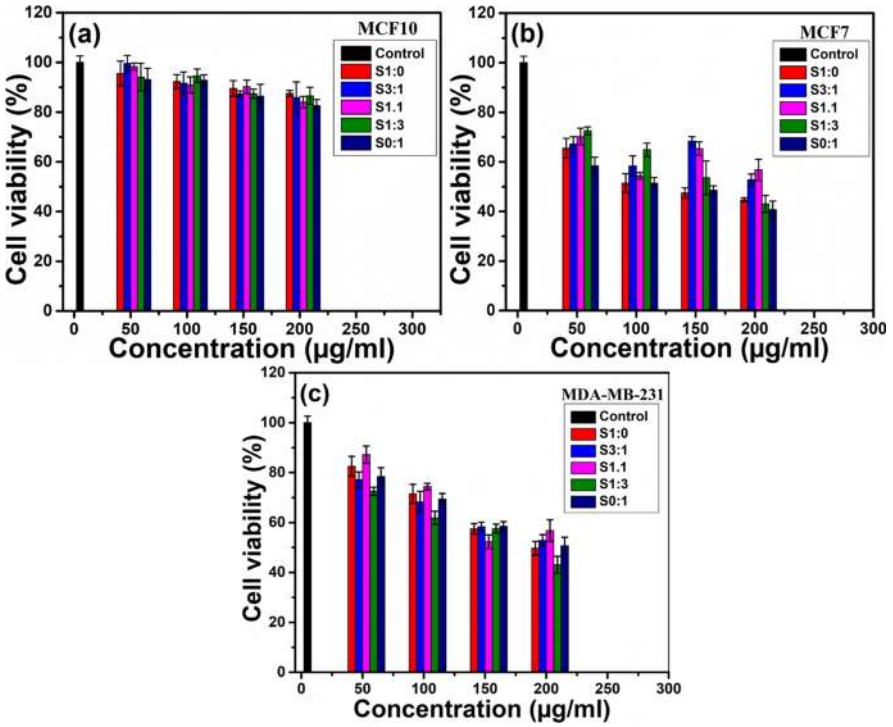

Figure 6. Cell viability profiles after treating with different concentrations of MNCs after 48 h of incubation period; (a) MCF-10, (b) MCF-7, and (c) MDA-MB-231.

effect of different cell lines *in vitro*. It was found that the nanoparticles are biocompatible as experimented in MCF-10 (Figure 6a). Conversely, MCF-7 and MDA-MB-231 treated with MNCs showed a significant decrease in cell viability. The cell viability of MCF-7 and MDA-MB-231 significantly decreased to ∼50 and 60%, respectively, when treated with MNCs at a concentration of 200 μg mL^{-1} (Figure 6b,c). The different responses of MDA-MB-231 and MCF-7 cell lines toward the cytotoxicity are possibly due to the difference in their molecular mechanisms. The cell death may be due to the reactive oxygen species (ROS) generation by $MnFe_2O_4$, which are very toxic toward the cancer cells and can be explained as follows: in acidic cancer cell pH (∼4−5), $MnFe_2O_4$ may disintegrate into Mn^{2+}, Fe^{2+}, and Fe^{3+} ions. The resulting leached Mn^{2+} ions play a prime role in the generation of ROS by dissociating H_2O_2 present in the mitochondria into hydroperoxyl ($HOO^{\bullet}$) and hydroxyl ($HO^{\bullet}$) radicals through Fenton's reaction.[60,61] The possible mechanism is outlined below

$$Mn^{2+} + H_2O_2 \rightarrow Mn^{3+} + HO^{\bullet} + OH^{-}$$

$$H_2O_2 + HO^{\bullet} \rightarrow H_2O + HOO^{\bullet}$$

$$Mn^{3+} + HOO^{\bullet} \rightarrow Mn^{2+} + H^{+} + O_2$$

Similar behaviors were found in earlier research as well.[6,62−64] Another possible reason can be due to ferroptosis, that is, iron-dependent cell death caused by lipid peroxidation. The Fe^{2+} or Fe^{3+} ion release from $MnFe_2O_4$ in the tumor site is more pronounced than that at the normal tissue. Released iron can participate in the Fenton reaction and induce ferroptosis of the tumor cell.[62,65,66] S0:1 possesses a relatively higher cytotoxicity effect, which may be due to the irregular shape and the decrease in the nanoparticle size, resulting in more surface area to react with the cells. The microscopy images of the normal and cancer cells after incubation with MNCs at the concentration of 200 μg evidence that the breast cancer cells were gone through the necrosis process (Supporting Information, Figure S8).

3.5. MRI Relaxation Properties of MNCs Using Phantom Agar Gel. The T_2-contrast ability of MNCs was evaluated by measuring $r2$ relaxivity at different metal ion concentrations of 0.25 to 1 mM. The data obtained from BRUKER 7 Tesla Animal MRI were exported to Matlab software (Mathworks, Natick, MA), and T_2 mapping was done using a nonlinear regression algorithm to calculate the relaxation time. Then, $r2$ relaxivities were calculated from the slope of the graph plotted with $1/T_2$ versus metal ion concentration, as shown in Figure 7a. The inverse relaxation time with respect to the sample concentration was calculated by

$$R_{1,2}C = \frac{1}{T_{1,2}(C)} - \frac{1}{T_{1,2}(0)}$$

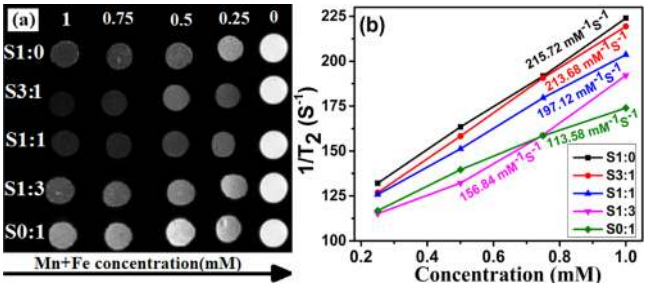

Figure 7. (a) T_2 imaging of MNCs in 1.5% agar solution at different concentrations and (b) plot of transverse relaxivity ($r2$) against Mn + Fe concentration (mM).

https://dx.doi.org/10.1021/acsomega.0c05382
ACS Omega 2021, 6, 5266−5275

12where R_1 and R_2 are the longitudinal and transverse relaxivities, respectively; C is the concentration; and $T_1(0)$ and $T_2(0)$ are the proton relaxation times.[67,68] It is observed that there is a decrease in T_2 time and the image contrast gets darker with an increase in concentration. The $r2$ values calculated from the plot of $1/T_2$ versus Mn + Fe concentration are illustrated in Figure 7b. The $r2$ values are found to be 215.72, 213.68, 197.12, 156.84, and 113.58 mM^{-1} s^{-1} for S1:0, S3:1, S1:1, S1:3, and S0:1, respectively. The relaxivity is directly proportional to the concentration and saturation magnetization M_s of the particle, and hence, S1:0 shows a higher $r2$ value. The obtained $r2$ values are comparable to those of the commercially available products resovist (151.95 mM^{-1} s^{-1}), ferumoxytol (84.9 mM^{-1} s^{-1}), ferumoxtran (160 mM^{-1} s^{-1}), and ferucarbotran (239.2 mM^{-1} s^{-1}).[69,70] This proves that MNCs have the ability to produce significant contrast in body tissues.

4. CONCLUSIONS

The PEGylated manganese ferrite nanoparticles processed by the solvothermal method showed morphological changes with variation in solvent ratios. Cubic-shape particles have been formed in the water solvent, and the size as well as morphology of the particle changed with the addition of ethanol due to the variation in dielectric constant and surface tension of the solvent. PEG-diacid coating on the nanoparticles provided colloidal stability suitable for biomedical applications. The nanoparticles possessed high saturation magnetization (M_s) and low coercivity (H_c) values, indicating a ferromagnetic behavior. A variation in coercivity and magnetization in MNCs occurred possibly due to the shape anisotropy. The MNCs exhibited better SAR values due to superior magnetic properties which depend not only on the concentration of the MNCs but also on the applied AMF of various field strengths at a constant frequency of 316 kHz. With an increase in concentration of MNCs and field strength, the SAR values increased significantly due to the increase in dipolar interactions. MNCs possess improved $r2$ relaxivity, which is proportional to the concentration and saturation magnetization M_s of the particle. The SAR and relaxivity are comparable to those of commercially available materials. The cytotoxicity study conducted in breast cancer cells (MCF-7 and MDA-MB-231) and normal epithelial cell MCF-10 cell lines revealed that the MNCs are biocompatible but possessed a significant toxic effect to breast cancer cells, probably due to generation of ROS and/or ferroptosis. The MHT, MRI, and *in vitro* studies ensure the potential application of $MnFe_2O_4$ nanoparticles in cancer theranostics.

5. MATERIALS AND METHODS

Analytical-grade chemicals were used as received. Iron(III) chloride hexahydrate ($FeCl_3{\cdot}6H_2O$, 98.9% purity), manganese chloride(II) tetrahydrate ($MnCl_2{\cdot}4H_2O$, 98%), ammonium hydroxide (NH_4OH), poly(ethylene glycol)-*bis*(carboxymethyl)ether (PEG-diacid, M_w = 600), phalloidin−tetramethylrhodamine B-isothiocyanate conjugates, MTT (98%), and 4,6-diamidino-2-phenylindole (DAPI, 98%) were purchased from Sigma-Aldrich. Antimycotic, antibiotic solutions and DMEM were obtained from Hi-Media.

In a typical synthesis procedure, 702.45 mg of $FeCl_3{\cdot}6H_2O$ and 161.87 mg of $MnCl_2{\cdot}4H_2O$ and 5 g of PEG-diacid were mixed in 60 mL of the solvent in a round-bottom flask. The solvents used were DI water and ethanol in different volume ratios of 1:0, 3:1, 1:1, 1:3, and 0:1. The mixture was continuously stirred at room temperature under an inert atmosphere (N_2 gas) for 10 min. 5 mL of ammonium hydroxide was then injected into the mixture and stirred continuously for another 15 min. The contents were then transferred to a 100 mL Teflon line stainless-steel autoclave and kept in a furnace for 18 h at a temperature of 180 °C. Once the solution cooled down to room temperature, the material was collected using a magnetic separation method by washing in a water−ethanol mixture five times. The samples were allowed to dry at room temperature under vacuum conditions. The dried-up nanoparticles formed were named S1:0, S3:1, S1:1, S1:3, and S0:1, respectively, for 1:0, 3:1, 1:1, 1:3, and 0:1 volume ratios of water and ethanol used during the reaction.

■ ASSOCIATED CONTENT

Supporting Information

The Supporting Information is available free of charge at https://pubs.acs.org/doi/10.1021/acsomega.0c05382.

Rietveld refinement for XRD, FTIR patterns of MNCs, hydrodynamic diameter and zeta potential of MNCs obtained from DLS, particle size distribution from FESEM images, N_2 adsorption−desorption isotherms, slope values calculated from the temperature versus time plot, time versus temperature plot and SAR values of the different MNCs at AMF of a field strength of 15 kA m^{-1}, TEM image of the sample S1:0, and optical microscopy images of cell lines after treatment (PDF)

■ AUTHOR INFORMATION

Corresponding Author

Niroj Kumar Sahu − *Centre for Nanotechnology Research, Vellore Institute of Technology, Vellore 632014, Tamil Nadu, India;* orcid.org/0000-0002-0499-4108; Email: nirojs@vit.ac.in, sniroj.phy@gmail.com

Authors

Chandunika R. Kalaiselvan − *Centre for Nanotechnology Research, Vellore Institute of Technology, Vellore 632014, Tamil Nadu, India*

Nanasaheb D. Thorat − *Medical Science Division, Nuffield Department of Women's & Reproductive Health, John Radcliffe Hospital, University of Oxford, Oxford OX3 9DU, U.K.;* orcid.org/0000-0001-6343-527X

Complete contact information is available at: https://pubs.acs.org/10.1021/acsomega.0c05382

Notes

The authors declare no competing financial interest.

■ ACKNOWLEDGMENTS

The authors gratefully acknowledge the financial support from DST- SERB, Government of India (project grant no. ECR/2016/000301).

■ REFERENCES

(1) Mornet, S. p.; Vasseur, S. b.; Grasset, F.; Duguet, E. Magnetic nanoparticle design for medical diagnosis and therapy. *J. Mater. Chem.* **2004**, *14*, 2161−2175.

(2) Giri, J.; Pradhan, P.; Somani, V.; Chelawat, H.; Chhatre, S.; Banerjee, R.; Bahadur, D. Synthesis and characterizations of water-based ferrofluids of substituted ferrites [$Fe_{1-x}B_xFe_2O_4$, B=Mn, Co (x=0−1)] for biomedical applications. *J. Magn. Magn. Mater.* **2008**, *320*, 724−730.
(3) Lee, J.-H.; Jang, J.-t.; Choi, J.-s.; Moon, S. H.; Noh, S.-h.; Kim, J.-w.; Kim, J.-G.; Kim, I.-S.; Park, K. I.; Cheon, J. Exchange-coupled magnetic nanoparticles for efficient heat induction. *Nat. Nanotechnol.* **2011**, *6*, 418−422.
(4) Lim, E.-K.; Huh, Y.-M.; Yang, J.; Lee, K.; Suh, J.-S.; Haam, S. pH-triggered drug-releasing magnetic nanoparticles for cancer therapy guided by molecular imaging by MRI. *Adv. Mater.* **2011**, *23*, 2436−2442.
(5) Kumar, S.; Daverey, A.; Khalilzad-Sharghi, V.; Sahu, N. K.; Kidambi, S.; Othman, S. F.; Bahadur, D. Theranostic fluorescent silica encapsulated magnetic nanoassemblies for in vitro MRI imaging and hyperthermia. *RSC Adv.* **2015**, *5*, 53180−53188.
(6) Patil, R. M.; Thorat, N. D.; Shete, P. B.; Otari, S. V.; Tiwale, B. M.; Pawar, S. H. In vitro hyperthermia with improved colloidal stability and enhanced SAR of magnetic core/shell nanostructures. *Mater. Sci. Eng., C* **2016**, *59*, 702−709.
(7) Jardim, K. V.; Palomec-Garfias, A. F.; Andrade, B. Y. G.; Chaker, J. A.; Báo, S. N.; Márquez-Beltrán, C.; Moya, S. E.; Parize, A. L.; Sousa, M. H. Novel magneto-responsive nanoplatforms based on $MnFe_2O_4$ nanoparticles layer-by-layer functionalized with chitosan and sodium alginate for magnetic controlled release of curcumin. *Mater. Sci. Eng., C* **2018**, *92*, 184−195.
(8) Salunkhe, A.; Khot, V.; Patil, S. I.; Tofail, S. A. M.; Bauer, J.; Thorat, N. D. MRI Guided Magneto-chemotherapy with High-Magnetic-Moment Iron Oxide Nanoparticles for Cancer Theranostics. *ACS Appl. Bio Mater.* **2020**, *3*, 2305−2313.
(9) Lee, J.-H.; Huh, Y.-M.; Jun, Y.-w.; Seo, J.-w.; Jang, J.-t.; Song, H.-T.; Kim, S.; Cho, E.-J.; Yoon, H.-G.; Suh, J.-S.; Cheon, J. Artificially engineered magnetic nanoparticles for ultra-sensitive molecular imaging. *Nat. Med.* **2007**, *13*, 95−99.
(10) Kim, J. H.; Kim, M.-J.; Park, Y. N.; Lee, J. T.; Kim, B. R.; Chung, J. B.; Choi, J. S.; Kim, K. S.; Kim, K. W. Mangafodipir trisodium-enhanced MRI of hepatocellular carcinoma: correlation with histological characteristics. *Clin. Radiol.* **2008**, *63*, 1195−1204.
(11) Small, W. C.; Macchi, D. D.; Parker, J. R.; Bernardino, M. E. Multisite study of the safety and efficacy of LumenHance, a new gastrointestinal contrast agent for MRI of the abdomen and pelvis. *Acad. Radiol.* **1998**, *5*, S147−S150.
(12) Pradhan, P.; Giri, J.; Banerjee, R.; Bellare, J.; Bahadur, D. Preparation and characterization of manganese ferrite-based magnetic liposomes for hyperthermia treatment of cancer. *J. Magn. Magn. Mater.* **2007**, *311*, 208−215.
(13) Tartaj, P.; González-Carreño, T.; Serna, C. J. Magnetic Behavior of γ-Fe_2O_3 Nanocrystals Dispersed in Colloidal Silica Particles. *J. Phys. Chem. B* **2003**, *107*, 20−24.
(14) Puntes, V. F.; Krishnan, K. M.; Alivisatos, A. P. Colloidal nanocrystal shape and size control: the case of cobalt. *Science* **2001**, *291*, 2115−2117.
(15) Margeat, O.; Tran, M.; Spasova, M.; Farle, M. Magnetism and structure of chemically disordered $FePt_3$ nanocubes. *Phys. Rev. B: Condens. Matter Mater. Phys.* **2007**, *75*, 134410.
(16) Jana, N. R.; Chen, Y.; Peng, X. Size- and Shape-Controlled Magnetic (Cr, Mn, Fe, Co, Ni) Oxide Nanocrystals via a Simple and General Approach. *Chem. Mater.* **2004**, *16*, 3931−3935.
(17) Sayed, F. N.; Polshettiwar, V. Facile and Sustainable Synthesis of Shaped Iron Oxide Nanoparticles: Effect of Iron Precursor Salts on the Shapes of Iron Oxides. *Sci. Rep.* **2015**, *5*, 9733.
(18) Zhou, Z.; Zhu, X.; Wu, D.; Chen, Q.; Huang, D.; Sun, C.; Xin, J.; Ni, K.; Gao, J. Anisotropic Shaped Iron Oxide Nanostructures: Controlled Synthesis and Proton Relaxation Shortening Effects. *Chem. Mater.* **2015**, *27*, 3505−3515.
(19) Cotin, G.; Kiefer, C.; Perton, F.; Ihiawakrim, D.; Blanco-Andujar, C.; Moldovan, S.; Lefevre, C.; Ersen, O.; Pichon, B.; Mertz, D.; Bégin-Colin, S. Unravelling the Thermal Decomposition Parameters for The Synthesis of Anisotropic Iron Oxide Nanoparticles. *Nanomaterials (Basel)* **2018**, *8*, 881.
(20) Kim, B. H.; Hackett, M. J.; Park, J.; Hyeon, T. Synthesis, Characterization, and Application of Ultrasmall Nanoparticles. *Chem. Mater.* **2014**, *26*, 59−71.
(21) Salazar-Alvarez, G.; Qin, J.; Šepelák, V.; Bergmann, I.; Vasilakaki, M.; Trohidou, K. N.; Ardisson, J. D.; Macedo, W. A. A.; Mikhaylova, M.; Muhammed, M.; Baró, M. D.; Nogués, J. Cubic versus Spherical Magnetic Nanoparticles: The Role of Surface Anisotropy. *J. Am. Chem. Soc.* **2008**, *130*, 13234−13239.
(22) Chinnasamy, C. N.; Jeyadevan, B.; Shinoda, K.; Tohji, K.; Djayaprawira, D. J.; Takahashi, M.; Joseyphus, R. J.; Narayanasamy, A. Unusually high coercivity and critical single-domain size of nearly monodispersed CoFe2O4 nanoparticles. *Appl. Phys. Lett.* **2003**, *83*, 2862−2864.
(23) Zhou, Z.; Zhao, Z.; Zhang, H.; Wang, Z.; Chen, X.; Wang, R.; Chen, Z.; Gao, J. Interplay between Longitudinal and Transverse Contrasts in Fe_3O_4 Nanoplates with (111) Exposed Surfaces. *ACS Nano* **2014**, *8*, 7976−7985.
(24) Lee, N.; Choi, Y.; Lee, Y.; Park, M.; Moon, W. K.; Choi, S. H.; Hyeon, T. Water-dispersible ferrimagnetic iron oxide nanocubes with extremely high r(2) relaxivity for highly sensitive in vivo MRI of tumors. *Nano Lett.* **2012**, *12*, 3127−3131.
(25) Zhao, Z.; Zhou, Z.; Bao, J.; Wang, Z.; Hu, J.; Chi, X.; Ni, K.; Wang, R.; Chen, X.; Chen, Z.; Gao, J. Octapod iron oxide nanoparticles as high-performance T(2) contrast agents for magnetic resonance imaging. *Nat. Commun.* **2013**, *4*, 2266.
(26) Massart, R.; Dubois, E.; Cabuil, V.; Hasmonay, E. Preparation and properties of monodisperse magnetic fluids. *J. Magn. Magn. Mater.* **1995**, *149*, 1−5.
(27) Tartaj, P.; Serna, C. J. Microemulsion-Assisted Synthesis of Tunable Superparamagnetic Composites. *Chem. Mater.* **2002**, *14*, 4396−4402.
(28) Guardia, P.; Pérez, N.; Labarta, A.; Batlle, X. Controlled Synthesis of Iron Oxide Nanoparticles over a Wide Size Range. *Langmuir* **2010**, *26*, 5843−5847.
(29) Viau, G.; Fiévet-Vincent, F.; Fiévet, F. Monodisperse iron-based particles: precipitation in liquid polyols. *J. Mater. Chem.* **1996**, *6*, 1047−1053.
(30) Li, X.-H.; Xu, C.-L.; Han, X.-H.; Qiao, L.; Wang, T.; Li, F.-S. Synthesis and Magnetic Properties of Nearly Monodisperse $CoFe_2O_4$ Nanoparticles Through a Simple Hydrothermal Condition. *Nanoscale Res. Lett.* **2010**, *5*, 1039.
(31) Suslick, K. S.; Fang, M.; Hyeon, T. Sonochemical Synthesis of Iron Colloids. *J. Am. Chem. Soc.* **1996**, *118*, 11960−11961.
(32) Massart, R. Preparation of aqueous magnetic liquids in alkaline and acidic media. *IEEE Trans. Magn.* **1981**, *17*, 1247−1248.
(33) Hufschmid, R.; Arami, H.; Ferguson, R. M.; Gonzales, M.; Teeman, E.; Brush, L. N.; Browning, N. D.; Krishnan, K. M. Synthesis of phase-pure and monodisperse iron oxide nanoparticles by thermal decomposition. *Nanoscale* **2015**, *7*, 11142−11154.
(34) Bronstein, L. M.; Huang, X.; Retrum, J.; Schmucker, A.; Pink, M.; Stein, B. D.; Dragnea, B. Influence of Iron Oleate Complex Structure on Iron Oxide Nanoparticle Formation. *Chem. Mater.* **2007**, *19*, 3624−3632.
(35) Sun, S.; Zeng, H.; Robinson, D. B.; Raoux, S.; Rice, P. M.; Wang, S. X.; Li, G. Monodisperse MFe_2O_4 (M = Fe, Co, Mn) Nanoparticles. *J. Am. Chem. Soc.* **2004**, *126*, 273−279.
(36) Chen, Z. Size and Shape Controllable Synthesis of Monodisperse Iron Oxide Nanoparticles by Thermal Decomposition of Iron Oleate Complex. *Synth. React. Inorg., Met.-Org., Nano-Met. Chem.* **2012**, *42*, 1040−1046.
(37) Wyman, J. The dielectric constant of mixtures of ethyl alcohol and water from -5 to 40°. *J. Am. Chem. Soc.* **1931**, *53*, 3292−3301.
(38) Yang, Z.; Xu, J.; Zhang, W.; Liu, A.; Tang, S. Controlled synthesis of CuO nanostructures by a simple solution route. *J. Solid State Chem.* **2007**, *180*, 1390−1396.
(39) Mullin, J. W. Crystallisation, 4th edition; Butterworth Heinemann. *Org. Process Res. Dev.* **2002**, *6*, 201−202.

https://dx.doi.org/10.1021/acsomega.0c05382
ACS Omega 2021, 6, 5266−5275

(40) Manoli, F.; Kanakis, J.; Malkaj, P.; Dalas, E. The effect of aminoacids on the crystal growth of calcium carbonate. *J. Cryst. Growth* **2002**, *236*, 363−370.
(41) Findenegg, G. H. J. N. Israelachvili: Intermolecular and Surface Forces (With Applications to Colloidal and Biological Systems). *Ber. Bunsenges. Physik. Chem.* **1986**, *90*, 1241−1242.
(42) Závišová, V.; Koneracká, M.; Múčková, M.; Lazová, J.; Juríková, A.; Lancz, G.; Tomašovičová, N.; Timko, M.; Kováč, J.; Vávra, I.; Fabián, M.; Feoktystov, A. V.; Garamus, V. M.; Avdeev, M. V.; Kopčanský, P. Magnetic fluid poly(ethylene glycol) with moderate anticancer activity. *J. Magn. Magn. Mater.* **2011**, *323*, 1408−1412.
(43) Barick, K. C.; Sharma, A.; Shetake, N. G.; Ningthoujam, R. S.; Vatsa, R. K.; Babu, P. D.; Pandey, B. N.; Hassan, P. A. Covalent Bridging of Surface Functionalized Fe_3O_4 and YPO_4: Eu Nanostructures for Simultaneous Imaging and Therapy. *Dalton Trans* **2015**, *44*, 14686−14696.
(44) Sahu, N. K.; Shanta Singh, N.; Ningthoujam, R. S.; Bahadur, D. Ce3+-Sensitized GdPO4:Tb3+ Nanorods: An Investigation on Energy Transfer, Luminescence Switching, and Quantum Yield. *ACS Photonics* **2014**, *1*, 337−346.
(45) Yamazaki, M.; Ito, T. Deformation and instability of membrane structure of phospholipid vesicles caused by osmophobic association: mechanical stress model for the mechanism of poly(ethylene glycol)-induced membrane fusion. *Biochemistry* **1990**, *29*, 1309−1314.
(46) Sahoo, B.; Bhattacharya, A.; Fu, H.; Gao, W.; Gross, R. A. Influence of PEG Endgroup and Molecular Weight on Its Reactivity for Lipase-Catalyzed Polyester Synthesis. *Biomacromolecules* **2006**, *7*, 1042−1048.
(47) Burger, K., *Solvation, ionic, and complex formation reactions in non-aqueous solvents : experimental methods for their investigation.* Elsevier Scientific Pub. Co.; Akadémiai Kiadó: Distribution for the U.S.A. and Canada, Elsevier/North-Holland, Amsterdam; New York; Budapest, Hungary; New York, N.Y., 1983.
(48) Liang, X.; Wang, X.; Zhuang, J.; Chen, Y.; Wang, D.; Li, Y. Synthesis of Nearly Monodisperse Iron Oxide and Oxyhydroxide Nanocrystals. *Adv. Funct. Mater.* **2006**, *16*, 1805−1813.
(49) Thommes, M.; Kaneko, K.; Neimark, A. V.; Olivier, J. P.; Rodriguez-Reinoso, F.; Rouquerol, J.; Sing, K. S. W. Physisorption of gases, with special reference to the evaluation of surface area and pore size distribution (IUPAC Technical Report). *Pure Appl. Chem.* **2015**, *87*, 1051−1069.
(50) Ayyappan, S.; Philip, J.; Raj, B. A facile method to control the size and magnetic properties of $CoFe_2O_4$ nanoparticles. *Mater. Chem. Phys.* **2009**, *115*, 712−717.
(51) Jeyadevan, B. Present status and prospects of magnetite nanoparticles-based hyperthermia. *J. Ceram. Soc. Jpn.* **2010**, *118*, 391−401.
(52) Atkinson, W. J.; Brezovich, I. A.; Chakraborty, D. P. Useable Frequencies in Hyperthermia with Thermal Seeds. *IEEE Trans. Biomed. Eng.* **1984**, *31*, 70−75.
(53) Joshi, R.; Perala, R.; Srivastava, M.; Singh, B.; Ningthoujam, R. Heat generation from magnetic fluids under alternating current magnetic field or induction coil for hyperthermia-based cancer therapy: Basic principle. *J. Radiat. Cancer Res.* **2019**, *10*, 156−164.
(54) Chandunika, R. K.; Rajagopalan, V.; Sahu, N. K. Synthesis of manganese doped β-FeOOH and MnFe2O4 nanorods for enhanced drug delivery and hyperthermia application. IET Nanobiotechnol. 2020, *14*, 823−829.
(55) Arteaga-Cardona, F.; Rojas-Rojas, K.; Costo, R.; Mendez-Rojas, M. A.; Hernando, A.; de la Presa, P. Improving the magnetic heating by disaggregating nanoparticles. *J. Alloys Compd.* **2016**, *663*, 636−644.
(56) Vamvakidis, K.; Katsikini, M.; Sakellari, D.; Paloura, E. C.; Kalogirou, O.; Dendrinou-Samara, C. Reducing the inversion degree of $MnFe_2O_4$ nanoparticles through synthesis to enhance magnetization: evaluation of their 1H NMR relaxation and heating efficiency. *Dalton Trans.* **2014**, *43*, 12754−12765.
(57) Makridis, A.; Topouridou, K.; Tziomaki, M.; Sakellari, D.; Simeonidis, K.; Angelakeris, M.; Yavropoulou, M. P.; Yovos, J. G.; Kalogirou, O. In vitro application of Mn-ferrite nanoparticles as novel magnetic hyperthermia agents. *J. Mater. Chem. B* **2014**, *2*, 8390−8398.
(58) Lanier, O. L.; Korotych, O. I.; Monsalve, A. G.; Wable, D.; Savliwala, S.; Grooms, N. W. F.; Nacea, C.; Tuitt, O. R.; Dobson, J. Evaluation of magnetic nanoparticles for magnetic fluid hyperthermia. *Int. J. Hyperther.* **2019**, *36*, 687−701.
(59) Razak, N. A.; Abu, N.; Ho, W. Y.; Zamberi, N. R.; Tan, S. W.; Alitheen, N. B.; Long, K.; Yeap, S. K. Cytotoxicity of eupatorin in MCF-7 and MDA-MB-231 human breast cancer cells via cell cycle arrest, anti-angiogenesis and induction of apoptosis. *Sci. Rep.* **2019**, *9*, 1514.
(60) Sahoo, B.; Sahu, S. K.; Nayak, S.; Dhara, D.; Pramanik, P. Fabrication of magnetic mesoporous manganese ferrite nanocomposites as efficient catalyst for degradation of dye pollutants. *Catal. Sci. Technol.* **2012**, *2*, 1367−1374.
(61) Xu, C.; Yuan, Z.; Kohler, N.; Kim, J.; Chung, M. A.; Sun, S. FePt Nanoparticles as an Fe Reservoir for Controlled Fe Release and Tumor Inhibition. *J. Am. Chem. Soc.* **2009**, *131*, 15346−15351.
(62) Sahu, N. K.; Gupta, J.; Bahadur, D. PEGylated FePt−Fe_3O_4 composite nanoassemblies (CNAs): in vitro hyperthermia, drug delivery and generation of reactive oxygen species (ROS). *Dalton Trans.* **2015**, *44*, 9103−9113.
(63) Neha, R.; Jaiswal, A.; Bellare, J.; Sahu, N. K. Synthesis of Surface Grafted Mesoporous Magnetic Nanoparticles for Cancer Therapy. *J. Nanosci. Nanotechnol.* **2017**, *17*, 5181−5188.
(64) Lesiak, B.; Rangam, N.; Jiricek, P.; Gordeev, I.; Tóth, J.; Kövér, L.; Mohai, M.; Borowicz, P. Surface Study of Fe3O4 Nanoparticles Functionalized With Biocompatible Adsorbed Molecules. *Front. Chem.* **2019**, *7*, 642.
(65) Wang, S.; Luo, J.; Zhang, Z.; Dong, D.; Shen, Y.; Fang, Y.; Hu, L.; Liu, M.; Dai, C.; Peng, S.; Fang, Z.; Shang, P. Iron and magnetic: new research direction of the ferroptosis-based cancer therapy. *Am. J. Cancer Res.* **2018**, *8*, 1933−1946.
(66) Patil, R. M.; Thorat, N. D.; Shete, P. B.; Bedge, P. A.; Gavde, S.; Joshi, M. G.; Tofail, S. A. M.; Bohara, R. A. Comprehensive cytotoxicity studies of superparamagnetic iron oxide nanoparticles. *Biochem. Biophys. Rep.* **2018**, *13*, 63−72.
(67) Gillis, P.; Koenig, S. H. Transverse relaxation of solvent protons induced by magnetized spheres: application to ferritin, erythrocytes, and magnetite. *Magn. Reson. Med.* **1987**, *5*, 323−345.
(68) Maenosono, S.; Suzuki, T.; Saita, S. Superparamagnetic FePt nanoparticles as excellent MRI contrast agents. *J. Magn. Magn. Mater.* **2008**, *320*, L79−L83.
(69) Lee, N.; Hyeon, T. Designed synthesis of uniformly sized iron oxide nanoparticles for efficient magnetic resonance imaging contrast agents. *Chem. Soc. Rev.* **2012**, *41*, 2575−2589.
(70) Thorat, N. D.; Bohara, R. A.; Malgras, V.; Tofail, S. A. M.; Ahamad, T.; Alshehri, S. M.; Wu, K. C.-W.; Yamauchi, Y. Multimodal Superparamagnetic Nanoparticles with Unusually Enhanced Specific Absorption Rate for Synergetic Cancer Therapeutics and Magnetic Resonance Imaging. *ACS Appl. Mater. Interfaces* **2016**, *8*, 14656−14664.

https://dx.doi.org/10.1021/acsomega.0c05382
ACS Omega 2021, 6, 5266−5275